ARTICLES

AIR–SEA INTERACTIONS FROM WESTERLY WIND BURSTS DURING THE NOVEMBER 2011 MJO IN THE INDIAN OCEAN

BY JAMES N. MOUM, SIMON P. DE SZOEKE, WILLIAM D. SMYTH, JAMES B. EDSON, H. LANGLEY DEWITT, AURÉLIE J. MOULIN, ELIZABETH J. THOMPSON, CHRISTOPHER J. ZAPPA, STEVEN A. RUTLEDGE, RICHARD H. JOHNSON, AND CHRISTOPHER W. FAIRALL

Observations from 1 km beneath to 25 km above the sea surface reveal the complex interactions in Indian Ocean westerly wind bursts associated with the Madden–Julian oscillation.

The Madden–Julian oscillation (MJO; Madden and Julian 1971, 1972) is a disturbance of the atmosphere over tropical oceans associated with surface westerly wind bursts, deep convection, and heavy precipitation. MJO convection typically initiates in the Indian Ocean, travels eastward at roughly 5 m s^{-1} along the equator until reaching the central Pacific, and then accelerates as it circumnavigates the globe with a recurrence period between 30 and 90 days (Zhang 2005). This phenomenon exerts a strong influence on Earth's weather and climate systems, acting globally on intraseasonal time scales (Zhang 2013). Yet MJO prediction is unsatisfactory, in large part because of insufficient representation of the multiscale processes in models. Parameterizations of these processes are limited by a lack of fundamental understanding, because of lack of adequate measurements. The contribution of atmosphere–ocean feedbacks to the emergence and evolution of the MJO remains unknown. This notion prompted the Dynamics of the Madden–Julian oscillation (DYNAMO; www.eol.ucar.edu/projects/dynamo/) hypothesis III (Yoneyama et al., 2013):

> The barrier layer, wind- and shear-driven mixing, shallow thermocline, and mixing-layer entrainment all play essential roles in MJO initiation in the Indian Ocean by controlling the upper-ocean heat content and SST, and thereby surface flux feedback.

AFFILIATIONS: MOUM, DE SZOEKE, SMYTH, AND MOULIN—College of Earth, Ocean and Atmospheric Sciences, Oregon State University, Corvallis, Oregon; EDSON—Department of Marine Sciences, University of Connecticut, Groton, Connecticut; DEWITT—NOAA/Pacific Marine Environmental Laboratory, Seattle, Washington; THOMPSON, RUTLEDGE, AND JOHNSON—Department of Atmospheric Sciences, Colorado State University, Fort Collins, Colorado; ZAPPA—Ocean and Climate Physics Division, Lamont-Doherty Earth Observatory, Columbia University, Palisades, New York; FAIRALL—NOAA/Earth System Research Laboratory, Boulder, Colorado
CORRESPONDING AUTHOR: James N. Moum, College of Earth, Ocean and Atmospheric Sciences, Oregon State University, Corvallis, OR 97331-5503
E-mail: moum@coas.oregonstate.edu
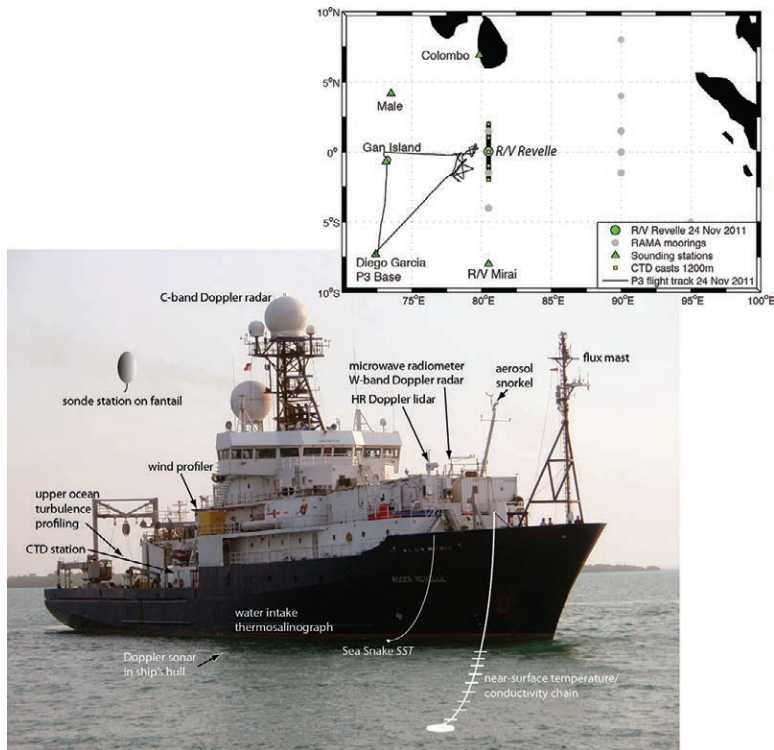
Fig. 1. Measurement systems installed on R/V *Roger Revelle* for DYNAMO. Inset map shows locations of land-based sounding stations, oceanographic moorings, and the research vessels *Mirai* and *Revelle* during the intensive observation period of DYNAMO. The black line outlines the flight track of the National Oceanic and Atmospheric Administration (NOAA) P3 research aircraft on 24 Nov 2011.

As part of the DYNAMO experiment conducted from boreal fall 2011 through early 2012 (Yoneyama et al. 2013), a particularly well-instrumented measurement program was conducted at the equator and 80.5°E from the research vessel *Roger Revelle* (Fig. 1) to make detailed observations of physical processes from 1 km below to 25 km above the sea surface. For as-yet-unknown reasons, the passage/occurrence of MJO convective envelopes observed at *Revelle* and elsewhere along the equator do not appear on a regular schedule (Zhang 2005). Between mid-October and mid-December, three cycles of the MJO were tracked across the Indian Ocean (Gottschalck et al. 2013; Yoneyama et al. 2013), and their active phases are identified here as MJO1, MJO2, MJO3. MJO2 was the strongest of the three. On 24 November 2011, MJO2 crossed the position of the *Revelle*. At the same time, a low-level cyclonic rotation to the immediate north, between the horn of India and *Revelle*, intensified. This region was identified by the U.S. Joint Tropical Warning Center (JTWC) as a tropical disturbance and upgraded to a tropical depression on 26 November. This event was forecast with a lead time

of 6 days and was not unexpected; nevertheless, it caused significant loss of life and property damage along Sri Lanka's southeast coast (see sidebar on the impact of tropical cyclone 05A on Sri Lanka).

At the equator, these atmospheric events resulted in a rapid decrease of sea surface temperature (SST). This was followed by a sustained period of warming moderated by the cooling effect of ocean turbulence. Our purpose here is to explore the physical processes behind these SST changes.

MEASUREMENTS. Instrumentation was installed on *Revelle* (Fig. 1; Table 1) to obtain the following:

- atmospheric soundings (eight per day) of velocity, temperature, relative humidity, and pressure altitude;
- complete atmospheric surface turbulent flux measurements for comparison to bulk formulas using standard meteorological observations;
- boundary layer velocity profile measurements using W-band Doppler radar and high-resolution Doppler lidar;
- continuous C-band Doppler radar scans measuring radial velocity and radar reflectivity;
- particle size distributions and chemical composition of aerosols;
- upper-ocean current profiles from hull-mounted Doppler sonar;
- water column optical profiles to determine the penetrating solar radiation, a key contributor to air–sea heat exchanges;
- sea surface (skin) temperature from infrared radiometers;
- near-surface ocean temperature and salinity profiles from ~0.05- to 7-m depth from a towed surface thermistor (SeaSnake) and fixed subsurface array (CT chain); and
- continuous profiling (150–200 casts per day) of upper-ocean temperature; salinity; microscale shear; and subsurface turbulent fluxes of heat, salt, and momentum.

Longer-time-scale context for these measurements was provided by the nearby equatorial Research Moored

Array for African–Asian–Australian Monsoon Analysis and Prediction (RAMA; McPhaden et al. 2009) buoy at 0°, 80.5°E, which was instrumented to provide measurements of basic surface meteorological fields and subsurface density and current structure.

Surface properties of the MJO at 0°, 80.5°E. The MJO is identified by large-scale, eastward-propagating negative anomalies of outgoing longwave radiation (OLR) at the top of the atmosphere, a quantity related to the depth of atmospheric convection. Several distinct features common among the three active MJO phases observed between October and December 2011 appear in Fig. 2. On the equator at 80.5°E,

active phases were associated with reduced OLR that persisted for periods of 5–10 days and coincide with reduced surface pressure (Fig. 2a), consistent with the findings of Madden and Julian (1972). Each active phase is associated with one or more westerly wind bursts of varying magnitude (Fig. 2b) followed quickly by an eastward acceleration of the ocean's near-surface zonal current (arrows in Fig. 2c).

Prior to the active phase of the MJOs, daily-averaged SST steadily increased [Fig. 2d shows *Revelle*-based SST computed from the near-surface temperature from the SeaSnake combined with the cool skin correction described in Fairall et al. (1996), as well as 1- and 5-m temperatures from the

## IMPACT OF TROPICAL CYCLONE 05A ON SRI LANKA

As the first westerly wind burst (WWB1) of MJO2 propagated eastward over the ship at 0°, 80.5°E, a cyclonic vortex was propagating westward 400–800 km to the north (Fig. SB1). According to the European Centre for Medium-Range Weather Forecasts (ECMWF) deterministic analysis, the vortex was at 4°N and directly north of *Revelle* at 1800 UTC 24 November, when the intense westerlies of the WWB1 near the equator and the westerly southern flank of the vortex coincided. This led to a significantly greater wind stress during WWB1 when the vortex was close to the ship, compared to that during WWB2.

On 25 November, southwesterly winds associated with the vortex caused severe weather at sea and considerable damage along the southern coast of Sri Lanka. Wind and intense rain were observed in Galle and Matara, where the sheared core of the vortex intersected the southern coast of Sri Lanka at 0600 UTC 26 November (Fig. SB1c), followed by sustained onshore winds exceeding 10 m s^{-1} (Fig. SB1d). The storm was responsible for casualties, including the loss of 33 lives, mostly of fishermen at sea in small boats.

The tropical disturbance subsequently intensified to 25-kt (13 m s^{-1}) winds and was identified as tropical depression TC05A off the southern cape of India by the U.S. Navy's Joint Typhoon Warning Center at 0000 UTC 26 November. TC05A propagated northwestward into the Arabian Sea, reaching tropical storm status on 28 November, with maximum sustained winds of 35 kt (18 m s^{-1}).

Though several numerical models predicted the formation of a large tropical disturbance south of Colombo, the fishermen had been provided no warning

of the storm. A discussion of the local effects of the storm and potential repercussions can be followed in archives of the Sri Lankan newspaper *The Sunday Times*. The suffering of the people of Sri Lanka illustrates the significance of timely prediction and warnings of severe weather.
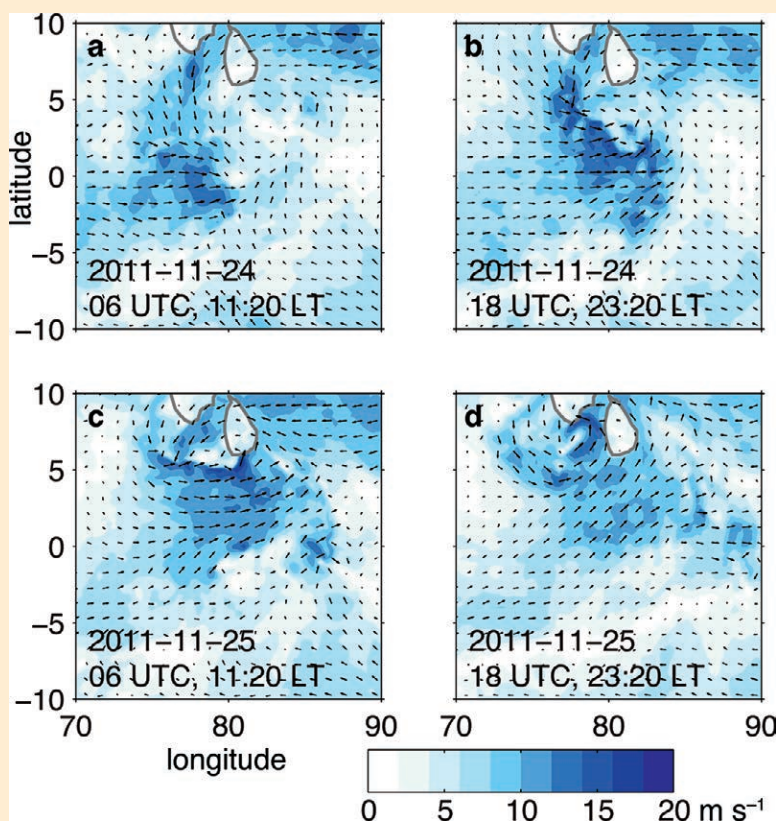
Fɪɢ. SB1. Surface wind vectors and speed (shaded) every 12 h (ECMWF deterministic analysis) illustrate eastward propagation of WWB1 across 80°E and centered on the equator coincident with westward propagation and intensification of a cyclonic vortex north of the equator across that longitude.

TABLE 1. List of measurements referred to in text, with responsible parties.

Instruments	Institution	Team leader	PI
Radiosondes Wind profiler	NCAR CSU	Bill Brown NCAR	Richard Johnson Colorado State University
Flux mast W-band Doppler Microwave radiometer SeaSnake Solar and IR radiometers Precipitation gauges	NOAA/ESRL Physical Science Division Oregon State University University of Connecticut	Dan Wolfe, Ludovic Bariteau NOAA/ESRL	Simon DeSzoeke (Oregon State University) James Edson (University of Connecticut) Chris Fairall (NOAA/ESRL)
Longwave radiometers	LDEO of Columbia University	Christopher Zappa (LDEO)	Christopher Zappa (LDEO)
High-resolution Doppler lidar	NOAA/ESRL Physical Science Division	Alan Brewer NOAA/ESRL	Alan Brewer NOAA/ESRL
C-band Doppler radar	Colorado State University	John Gerlach NASA GSFC	Steven Rutledge Colorado State University
Aerosol chemistry	NOAA/PMEL Atmospheric Chemistry Group	Derek Coffman, Langley DeWitt NOAA/PMEL	Timothy Bates NOAA/PMEL
Upper-ocean measurements	Oregon State University Ocean Mixing Group	James Moum Oregon State University	James Moum Oregon State University
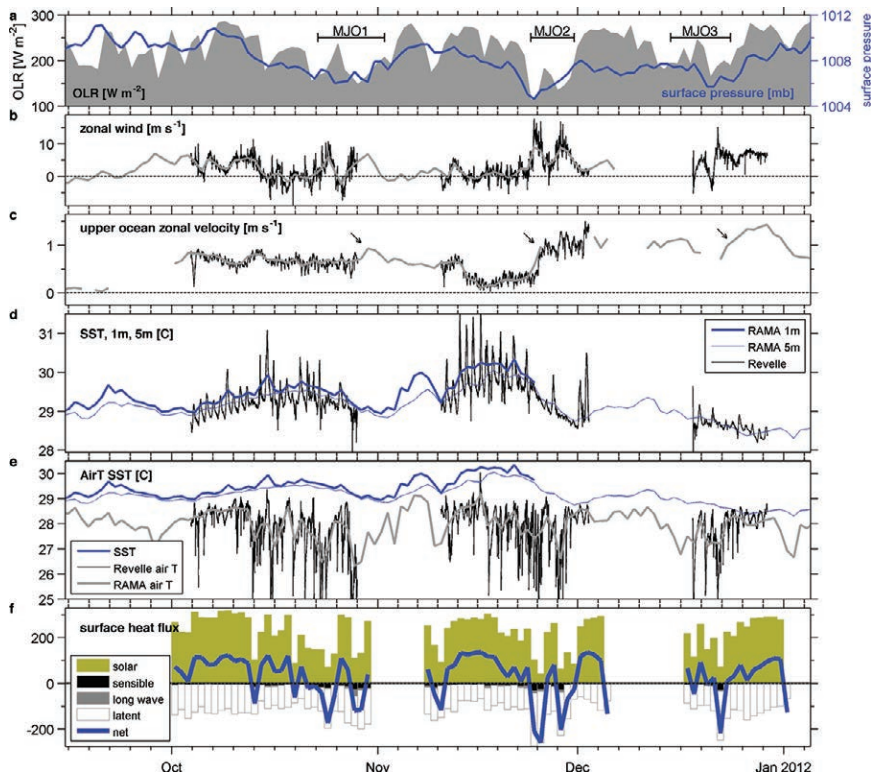
FIG. 2. Time series at 0°, 80.5°E during DYNAMO. (a) OLR (shaded) from the Advanced Very High Resolution Radiometer (AVHRR) instrument aboard the NOAA polar-orbiting spacecraft and surface pressure (blue line) from the nearby RAMA surface meteorological buoy. (b) Zonal wind speed. Ship (10-min averages; thin lines) and RAMA (daily averages; thick lines) measurements are shown for all series where available. (c) Upper-ocean zonal velocity at 20-m depth. (d) SST (black; near-surface temperature with cool skin correction applied based on Fairall et al. 1996); temperatures at 1 (thick blue) and 5 m (thin blue). (e) Air temperatures from *Revelle* and RAMA with SST repeated for direct comparison. (f) Surface heat fluxes partitioned into incoming solar radiation, outgoing longwave radiation, sensible heat, and latent heat. The fluxes are defined as positive down; values > 0 represent heating of the ocean by the atmosphere. All quantities shown are daily averages except for *Revelle*-based winds, ocean velocity, SST, and air temperature, which are 10-min averages.

nearby RAMA mooring]. When skies were clear and wind speed was low, the rapid-response ship-based measurements revealed daily peaks in near-surface warming of up to 3°C. Strong negative excursions in surface air temperature reflect the effect of cold downdrafts driven by evaporation of precipitation

(Fig. 2e). With the arrival of deep convection (low OLR) at the onset of the active phase, solar radiation at the sea surface decreased while wind-driven latent cooling increased at a rate of 0.5 W m^{-2} for each 1 W m^{-2} of solar flux reduction. Roughly corresponding to the active and suppressed phases of the MJO, the net surface heat flux changed sign from heating to cooling the sea surface (Fig. 2f).[1] This, plus the mixing of cool water from below, contributed to cooling of the upper ocean during active MJO events (see discussion related to Fig. 7).

Air temperature and SST both decreased in active phases of the MJO, with air temperature decreasing more than SST. Mean values of sea–air temperature difference increased from 0.9°C for days when net surface heat flux warmed the ocean to 1.6°C for days when net heat flux cooled the ocean (Fig. 2f). The sensible heat flux increased from 5 W m^{-2} on warming days to 17 W m^{-2} on cooling days because of an 80% increase in sea–air temperature difference, a 40% increase in wind speed, and more positive correlation of sea–air temperature difference with wind speed. Despite the decrease in air temperature, surface air specific humidity was the same on days when the ocean warmed as when it cooled. Latent heat flux increased ~30% from 96 W m^{-2} on warming days to 126 W m^{-2} on cooling days. Stronger wind speed and weaker negative covariance between wind speed and sea–air humidity difference are responsible for the stronger latent heat flux, despite a 6% decrease of sea–air specific humidity. Near-surface atmospheric cold pools occurred in both suppressed and active phases of the MJO but were stronger and more frequent during the active phase (Fig. 2e), with air–surface temperature differences exceeding 4°C (shown below).

Reductions in OLR and surface pressure were largest during MJO2, as were the strength of the wind bursts and the increased zonal current velocities in the direction of the wind. Furthermore, the net surface heat fluxes were most strongly negative and the reduction in SST was greatest during MJO2. *Revelle*
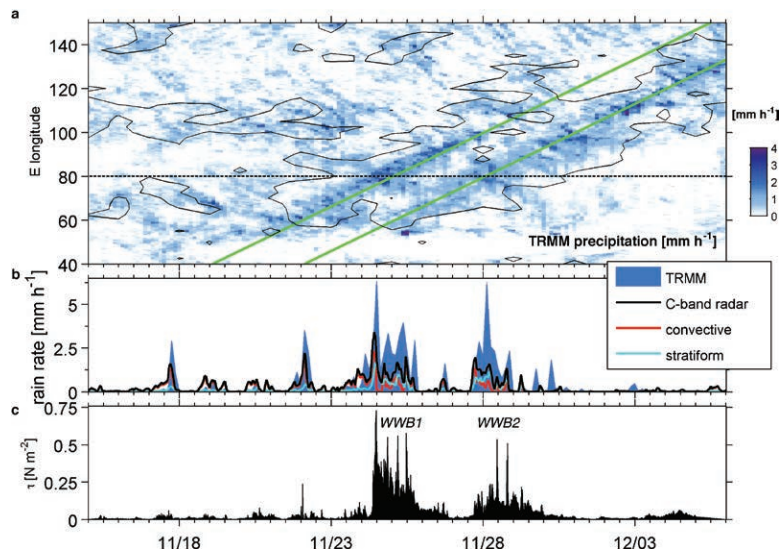
FIG. 3. (a) Hovmöller plot of TRMM precipitation at the equator and across the Indian Ocean for the period of MJO2 (blue image color); corresponding contours of OLR = 200 W m^{-2} (black). Green lines indicate propagating disturbances in TRMM at roughly the atmospheric Kelvin wave speed, 8.6 m s^{-1}. Note that the OLR signal travels more slowly than the rain signal. (b) Time series of precipitation from TRMM (blue shading; averaged ±0.5° both zonally and meridionally about the ship position at 0°, 80.5°E) and from shipboard C-band radar (black; convective and stratiform components are shown in off greens). Standard convective and stratiform echo partitioning methods (Steiner et al. 1995; Yuter and Houze 1998) were used with a 40-dBZ threshold. Separate $R(z)$ relationships derived from Gan Island two-dimensional optical video distrometer (2DVD) data during DYNAMO were employed to calculate hourly areal-average radar rainfall accumulation for each precipitation type. These relationships are $R_{CONV} = 0.034 z^{0.69}$ and $R_{STRAT} = 0.025 z^{0.64}$ (linear reflectivity units and mm h^{-1} rainfall units). All calculations were performed at 2-km height on gridded radar data (2-km horizontal and 0.5-km vertical resolution), out to 50-km range. (c) Time series of ship-measured wind stress (black shading).

was in an ideal observational position with all systems working to record the full extent of the atmospheric structure and oceanic response to MJO2. In the next two sections, we examine atmospheric and oceanic aspects of this event with the wide array of measurements available.

Atmospheric structure of the MJO2 wind bursts. A longitude–time Hovmöller plot of OLR averaged ±0.5° about the equator indicates MJO2 as an envelope of low OLR (Fig. 3; OLR within the closed black contour is less than 200 W m^{-2}) moving eastward with phase speed ~5 m s^{-1} that passed over *Revelle* between about 23 and 29 November (Yoneyama et al. 2013). The Tropical Rainfall Measuring Mission (TRMM)

---

[1] Positive heat fluxes warm the ocean.

precipitation signal in Fig. 3a (color shaded) identifies two convectively coupled or moist Kelvin waves moving at 8.6 m s^{-1} within the slower-moving envelope of low OLR that identifies MJO2 (Gottschalck et al. 2013). In time series from *Revelle*, each Kelvin wave is associated with a precipitating event (Fig. 3b) and simultaneous wind burst (Fig. 3c). Figure 3 thus illustrates the distinctive double wind burst and precipitation structure of MJO2. We refer to the two precipitation–wind events of MJO2 as westerly wind burst 1 (WWB1) on 24 November and westerly wind burst 2 (WWB2) on 28 November. The 10-min averaged wind stress magnitude at the leading edge of WWB1 exceeded 0.7 N m^{-2}, the largest value observed at 0°, 80.5°E during DYNAMO.

Most of the precipitation associated with MJO2 fell during the passage of the two Kelvin waves (Fig. 3b). Areal averaged daily precipitation within 100 km of *Revelle* was 37 mm during the 24-h period beginning at 0900 UTC 24 November, the largest 24-h accumulation observed on the equator by *Revelle* during DYNAMO.

C-band radar estimates of precipitation at *Revelle* show a series of rain events occurring irregularly about every 36 h, prior to the arrival of the WWBs. High radar reflectivity in these events indicate stronger precipitation originating from convective updrafts (Fig. 3b). Widespread stratiform precipitation (with moderate radar reflectivity) increased substantially following the leading edges of WWB1 and WWB2. During each wind burst, convective and stratiform rainfall contributed about equally to the total rainfall, whereas prior to the WWBs the rainfall was approximately 80% convective. The increased contribution of stratiform rainfall to total rainfall during MJO2 is consistent with previous studies of tropical precipitation over the ocean [Global Atmospheric Research Program (GARP) Atlantic Tropical Experiment (GATE; Bell and Suhasini 1994) and Tropical Ocean and Global Atmosphere Coupled Ocean–Atmosphere Response Experiment (TOGA COARE; Short et al. 1997)]. This observation implies a deep, "top heavy" profile of latent heating (Schumacher et al. 2004) during the WWBs: that is, heating at the top and cooling slightly in the boundary layer due to evaporating precipitation.

Atmospheric soundings from *Revelle* show potential temperature anomalies (θ; Fig. 4a), specific humidity anomalies (Fig. 4b), and zonal wind (Fig. 4c) associated with the two WWBs in MJO2. WWB1 was accompanied by a surface pressure drop and mean 8 cm s^{-1} upward velocity over the northern DYNAMO array, compared to WWB2 with mean upward

vertical velocity of 6 cm s^{-1} (Fig. 4a), consistent with precipitation in the WWBs (Johnson and Ciesielski 2013).

The time evolution of the soundings shows the effects of diurnal heating, lateral advection, and convection on the potential temperature and humidity. In the convectively suppressed period before the arrival of the WWBs (11–23 November), trade cumulus and cumulus congestus clouds increased the midtroposphere humidity (3–8 km; Fig. 4b). When the humidity in the upper troposphere was anomalously low (relative humidity below the 70% contour; thin line), descending potential temperature and zonal wind anomalies in the upper troposphere (~1 cm s^{-1} from 6 to 14 km on 11–18 November) suggest subsidence, advection of a tilted gradient structure past the ship, or a tilted wave response to convectively coupled Kelvin waves (Kiladis et al. 2009). In the week before the active phase of MJO2, the low to middle troposphere gradually moistened and the moisture occasionally reached deeper into the troposphere (Fig. 4b; e.g., on 17, 19, 20, and 22 November) presumably associated with intense convective rain events. The C-band radar measured convective rainstorms about every 1.5 days at this time (Fig. 3b). Specific humidity (Fig. 4b) in the middle and upper troposphere increased significantly above their average just prior to the onset of WWB1 (24 November) and WWB2 (28 November) and subsequently decreased during and immediately after the wind bursts. Maximum specific humidity anomalies were observed between 2 and 5 km, with large positive anomalies of up to 9 km during each WWB.

Zonal wind anomalies associated with the two westerly wind bursts arrived first at the surface and then penetrated to 8 km within one day (Fig. 4c). These two wind events were separated by one day of weak, easterly winds, with slightly drier air and little or no precipitation as seen on 26 November in Fig. 4b. This was presumably because dry air was advected into *Revelle*'s sampling domain, possibly associated with the synoptic-scale wind field surrounding the tropical cyclone to the north. Easterlies in the upper troposphere (Fig. 4c; 10–16 km) began at the onset of MJO2 and persisted for two weeks. While WWBs are commonly associated with MJO events, this particular separation of westerlies into two distinct bursts, as well as their vertical tilt during MJO2, bears the signature of convectively coupled Kelvin waves (Kiladis et al. 2009) propagating over the ship during MJO2 (Gottschalck et al. 2013). Such propagating disturbances are frequently associated with the active phase of the MJO, albeit

with larger phase speeds than are observed here (typically 10–17 m s⁻¹; Roundy 2008). The temperature and moisture structures of the two WWBs are consistent with that of convectively coupled Kelvin waves observed over the Pacific Ocean (Straub and Kiladis 2002; Kiladis et al. 2009). In both the Indian and Pacific basins, positive thermal and moisture anomalies have a westward tilt with height, as does the zonal wind anomaly. However, the phasing of the anomalies over the Indian Ocean differs slightly from that observed over the Pacific. In the lower troposphere, the positive moisture and temperature anomalies during the DYNAMO WWBs precede the zonal wind anomalies by approximately one and two days, respectively. Composites from Majuro in the western Pacific (Kiladis et al. 2009) show moisture
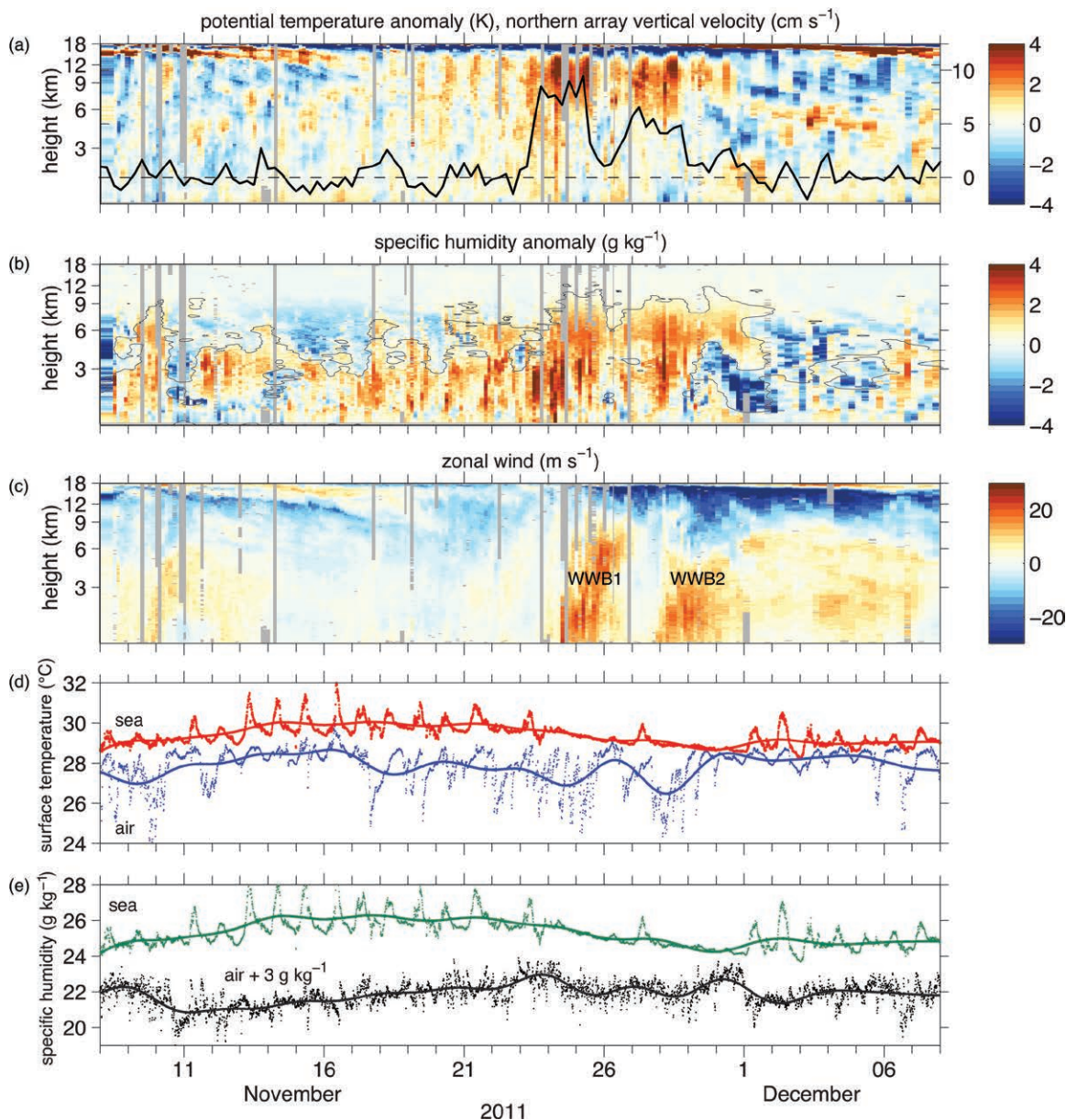
Fɪɢ. 4. (a) Potential temperature anomaly. (b) Specific humidity anomaly. (c) Zonal wind in the troposphere above the *Revelle* from rawinsondes. (d) Temperatures values at 10-m height and the sea surface. (e) Specific humidity values at 10-m and the sea surface. The vertical coordinate is mass weighted in (a)–(c). Anomalies are computed relative to mean *Revelle* soundings within 12° longitude and 5° latitude of the equatorial station at 80.5°W. Gray vertical lines indicate missing data. The 400-hPa vertical velocity computed from the northern array soundings (Johnson and Ciesielski 2013) is shown in (a) (right axis). The 2-day running averages are plotted in (d),(e) to provide the overall trends.
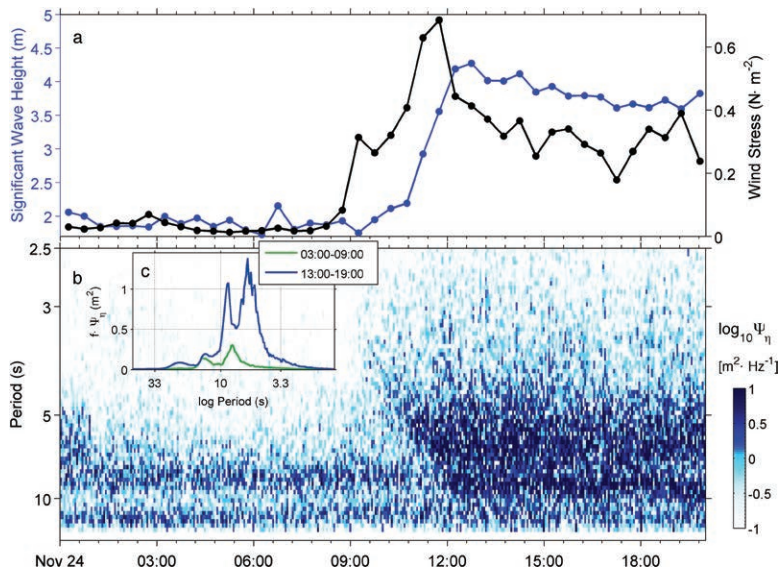
FIG. 5. Time series of wind and waves at *Revelle* showing the arrival of the first wind burst of MJO2. (a) Wind stress (black) and significant wave height (blue) as measured from motion-corrected laser altimeter. (b) Spectrogram of wave height. (c) Averaged spectra (in variance-preserving form) representing time intervals 6 h prior to the arrival of the wind burst (0300–0900 UTC) and 6 h following (1300–1900 UTC).

and temperature anomalies precede zonal wind by approximately two and three days, respectively. A day or two following the peak westerlies, drying is observed in the lower troposphere between 2 and 5 km (Fig. 4b), coinciding with prevalent stratiform precipitation (Fig. 3b). The evolution of the thermodynamic fields for both WWBs is consistent with the shipborne radar findings showing a transition from a dominance of convective precipitation at the beginning to stratiform precipitation during each WWB (Fig. 3).

Potential temperature anomalies in Fig. 4a are dominated by upper-tropospheric warm events associated with Kelvin waves, westerly wind bursts, and prolonged stratiform rain. Specific humidity anomalies are observed in the midtroposphere, below the strongest temperature anomalies. Latent heat of condensation in the midtroposphere nearly balances adiabatic cooling from upward motion, resulting in small temperature anomalies there. In the upper troposphere, two distinct positive potential temperature anomalies of about 3°C lead each of the WWBs by about one day. The warm anomalies last about three days each, and the potential temperature anomaly returns to nearly zero between the two warm anomalies. Potential temperature anomalies were small in the boundary layer and lower troposphere in the week preceding the active phase of

MJO2 (16–23 November). Gradual warming of the upper troposphere (2°C) and diurnal warming (~1°C each day) above 6 km were more subtle than the two warm anomalies associated with the stratiform rain in the WWBs. Surface westerly wind accelerates 5 m s⁻¹ day⁻¹ at the front of the deep convective events, implying local convergence at the *Revelle* that is much stronger than the convergence averaged over the northern sounding array.

Figure 4e shows gradual moistening near the ocean surface prior to 24 November, mirroring the response of the lower to middle troposphere. The specific humidity near the surface (Fig. 4e) and throughout the lower troposphere (Fig. 4c) decreased during the WWBs. The SST and corresponding value of the sea surface specific humidity began to decrease as the daily-averaged net heat flux changed sign around 21–22 November. This decrease is associated with the onset of the isolated rain events rather than the widespread deep convection and stratiform precipitation that began just prior to WWB1 on 24 November. The onset of zonal wind and sea surface cooling was observed nearly simultaneously with the deep convection, somewhat earlier than suggested by reanalysis in the Indian Ocean (Zhang 2005). An investigation of whether the timing of events in MJO2 is representative of the other active phases is ongoing.

Ocean response to wind bursts during MJO2. The leading edge of WWB1, identified by the initial increase in wind stress from the preceding calm conditions, arrived at *Revelle*'s site at 0900 UTC 24 November (Fig. 5a, black). Prior to this, the wave field was dominated by a two-component swell with periods 8 and 13 s, as seen in wave height spectra measured from a Reigl laser altimeter on *Revelle*'s bow (Fig. 5c, green). Directional wave spectra derived from ship's X-band radar via Wave Monitoring System (WaMoS) processing (Borge et al. 1999; Cifuentes-Lorenzen et al. 2013; Wyatt et al. 2003), not shown here, identify the 8- and 13-s swell components as coming from the north-northeast and the south-southwest, respectively.

Wind stress began to increase at about 0800 UTC to 0.3 N m⁻² by 0900 UTC, peaking at 0.7 N m⁻² at 1200 UTC (30-min averages shown in Fig. 5a). The

peak in significant wave height lagged that in wind stress by about 1 h. The spectrogram (Fig. 5b) shows the abrupt appearance of a narrowband wind-wave field at 0.25–0.30 Hz (3–4-s period) at 0900 UTC. The linear phase speed was only about one-half the wind speed, indicative of very young seas. Thereafter, the spectrum of the wind waves broadened in frequency and increased in intensity, masking the original two-component swell by 1200 UTC.

A clearer depiction of wave states before and after the arrival of WWB1 is seen in individual spectra (Fig. 5c; here in variance-preserving form, where equal areas represent equal energies). These emphasize the amplification of the higher-frequency wind-wave field and show the change in the lower-frequency swell components. The 13-s-period waves remained after the wind burst's arrival, but the 8-s swell was either replaced or overwhelmed by a 9-s swell from due west, the direction of WWB1. The contribution of the growing and breaking wind waves to marine aerosols in the lower atmosphere was significant (see sidebar on the aerosol response to WWB1).

The wind bursts' initial influence on the upper few meters of the ocean is seen in fast temperature sensors (FP07s) suspended from *Revelle*'s bow at 2.0, 3.9, and 7.1 m (Fig. 6). The net consequence of the MJO was to cool the sea surface (Fig. 2d), but the processes that modify SST were complex and cooling did not proceed uniformly in time. In particular, the cooling
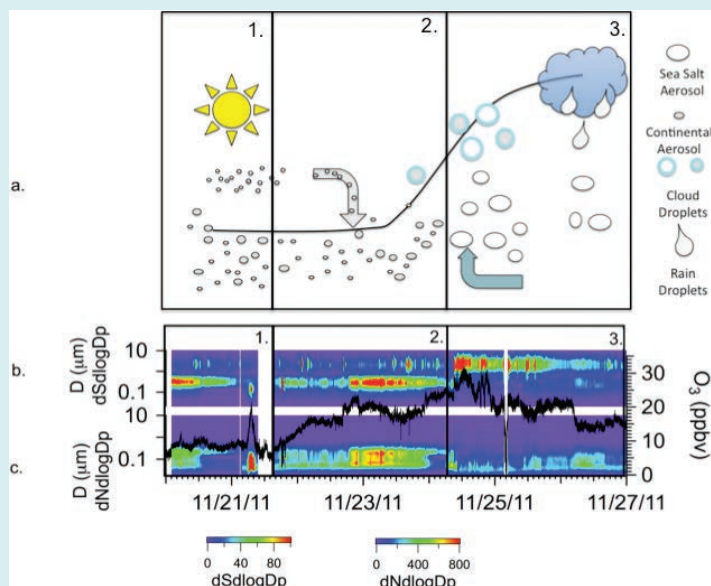
AEROSOL RESPONSE TO WWB1

Aerosols were sampled by a snorkel mounted above the bow deck (Fig. 1; DeWitt et al. 2013; Bates et al. 2005). Size distributions and chemical compositions were measured on a nearly continuous basis throughout the DYNAMO experiment. A schematic representation of the aerosol response to WWB1 reveals salient aspects of the aerosol evolution and suggests potential feedbacks between aerosol and convection in the remote Indian Ocean (Fig. SB2).

Before the convective phase of MJO2 and its associated wind bursts (stage 1 in Fig. SB2), low ozone levels and a buildup of submicron aerosols prevailed. The aerosol was determined to be of either continental or marine origin by prevailing aerosol transport directions and chemical composition. Higher submicron aerosol concentrations were measured from northerly (or continental) aerosol transport and lower for southerly (or clean marine) aerosol transport.

As convection intensified and became more frequent, air masses were injected from the upper atmosphere (stage 2), ozone levels rose, and submicron particles from aloft were introduced into the marine boundary layer. These submicron aerosols, primarily comprised of sulfate, have the potential to act as cloud condensation nuclei (CCN; Köhler 1936; Petters and Kreidenweis 2007). The sharp increase in wind speed of WWB1 (stage 3) lofted supermicron primary marine aerosol into the atmosphere while heavy rain simultaneously cleared the atmosphere of existing submicron aerosol. This increased the aerosol surface area and thus the potential scattering surface, raising the aerosol optical thickness while reducing the total aerosol number and thus potential CCN concentrations (Fig. SB2).

As demonstrated from these in situ aerosol measurements taken during the November MJO event, MJO-related convection had a significant effect on relative concentrations of submicron continental and marine aerosol and supermicron primary marine aerosol over the Indian Ocean (DeWitt et al. 2013). Changing aerosols translate into regional changes of the aerosol optical thicknesses and concentrations of available CCN in the remote Indian Ocean. Feedbacks to cloud formation, convective invigoration (Rosenfeld et al. 2008), and the atmosphere's radiative budget are intriguing issues for future research.

FɪG. SB2. (a) Schematic of aerosol response separated into three observed temporal stages of MJO passage at 0°, 80°E. (b) Log-normalized surface-area size distribution (*dS*d*log*Dp) of aerosols from 0.02 to 10 *µ*m. (c) Log-normalized number concentration of aerosols as a function of aerosol diameter (*dN*d*log*Dp). Color scales are shown at bottom. Overlaid on (b),(c) is ozone concentration in parts per billion by volume (ppbv) in black.
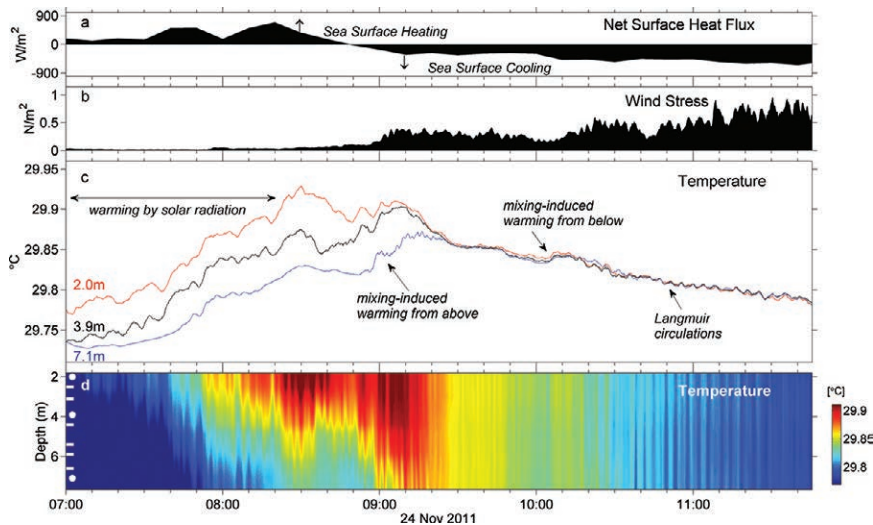
FIG. 6. Structure of the near surface of the ocean as the leading wind burst of MJO2 arrived at *Revelle*. (a) Net surface heat flux. (b) Surface wind stress. (c) Ocean temperature at 2.0, 3.9, and 7.1 m [depths denoted by white dots in (d)]. (d) Image-color plot of temperature in the upper 8 m from sensors at depths indicated at left and sampling as they are profiling the water column with wave motion.

of the upper ocean noted in Fig. 6 was interrupted by shorter-duration episodes of warming. Prior to 0800 UTC 24 November, net daytime surface heating created a warm layer in the upper several meters, with the heating rate being modulated by variations in solar radiation. This temperature structure is representative of the thin, near-surface diurnal warm layer of several degrees Celsius difference that dominates the high-frequency SST signal in Fig. 2d. Optical profiles of penetrating solar radiation made from *Revelle* (C. Ohlmann, University of California, Santa Barbara, 2013, personal communication) suggest that 50% of solar heat was trapped in the upper 1.5 m. Consequently, heating above 2 m was even more intense than at 2 m.

With the arrival of WWB1 on 24 November, the net surface heat flux changed sign and the daytime heating ended before 0900 UTC (sunset is roughly 1200 UTC at *Revelle*'s location). An immediate result was the downward mixing of heat from the thin, diurnally warmed layer at the surface to the sensors at 2.0, 3.9, and 7.1 m, which warmed during the first 15 min of the storm despite cooling from the atmosphere. Subsequent cooling of the upper 8 m was interrupted by a short heating event at 1000 UTC, associated with mixing of warm water from below, a consequence of the salt-stratified barrier layer (discussed below in reference to Fig. 7).

Shortly after 1000 UTC, temperature traces show a narrowband oscillation of alternating cool and warm fluid. The period, 3–4 min, is consistent with velocity signals measured by Doppler sonar. This oscillatory motion suggests the presence of Langmuir circulations, which reach to the base of the mixed layer, entrain fluid from there, and bring it to the surface. Langmuir circulations are a unique sea surface cooling mechanism not directly included in our measurements of subsurface turbulent heat flux (discussed later).

At greater depths, the influence of temperature and salinity stratification on MJO-related SST modification is revealed by time series of velocity, temperature, salinity, and turbulence dissipation rate from the Chameleon turbulence profiler (Moum et al. 1995; Figs. 7a–f). Before the arrival of WWB1, the upper 25 m of the water column was relatively warm and fresh and salinity dominated the stratification beneath the diurnal warm layer. At these salinities and temperatures, a 0.25-psu change in salinity contributes an equivalent change in density as a 0.60°C change in temperature. This represents a classical example of barrier-layer structure wherein the addition of saline stratification to thermal stratification complicates the ocean's response to surface forcing (McPhaden and Foltz 2013). Barrier layers may contribute to intensification of tropical cyclones by partially insulating the sea surface against cooling from below caused by subsurface mixing (Balaguru et al. 2012).

Details of the barrier-layer structure are shown in Figs. 7i,j, in which both isotherm and isohaline spacing represent equal contributions to density. It is evident that the halocline above 20-m depth dominated the stratification until about 1200 UTC. The warm layer centered around 20-m depth (Fig. 7i) was quickly mixed upward, contributing to the SST warming event evident around 1000 UTC (Fig. 6c). At the same time and despite heavy rainfall, sea surface salinity increased because of entrainment of salty water upward from the halocline. The halocline (and the mixed layer) deepened to the thermocline at 50-m depth almost 24 h after the arrival of WWB1.

At this stage, entrainment of cool fluid across the thermocline increased the rate of sea surface cooling, denoted by the change in slope of time-varying SST beginning just prior to 1200 UTC 25 November (Fig. 7h).

A curious feature is the presence of biologically generated turbulence during nighttime hours. This was associated with particularly energetic swimmers following the deep scattering layer comprised of zooplankton, which migrate down and out of the sunlit upper layers to avoid predators during the day then up into the euphotic zone to feed at night. The signal is seen in the abrupt increase in turbulent

dissipation at all depths above 60 m on the calm days (22 and 23 November) preceding WWB1 (Fig. 7f) and confirmed by comparison to volume backscatter estimates from high-frequency (120 kHz) acoustic measurements from a hull-mounted transducer. It has been observed that fish-aggregating devices (FADs) are particularly effective in the Indian Ocean (Moreno et al. 2007). It is likely that the ship acted as an FAD and that the observed biologically generated turbulence was a local rather than a dynamically significant effect. The signature of the turbulence due to the forcing of WWB1 was much more intense than the biogenic mixing, as evidenced by the deepening mixing that followed (and exceeded) the mixed-layer
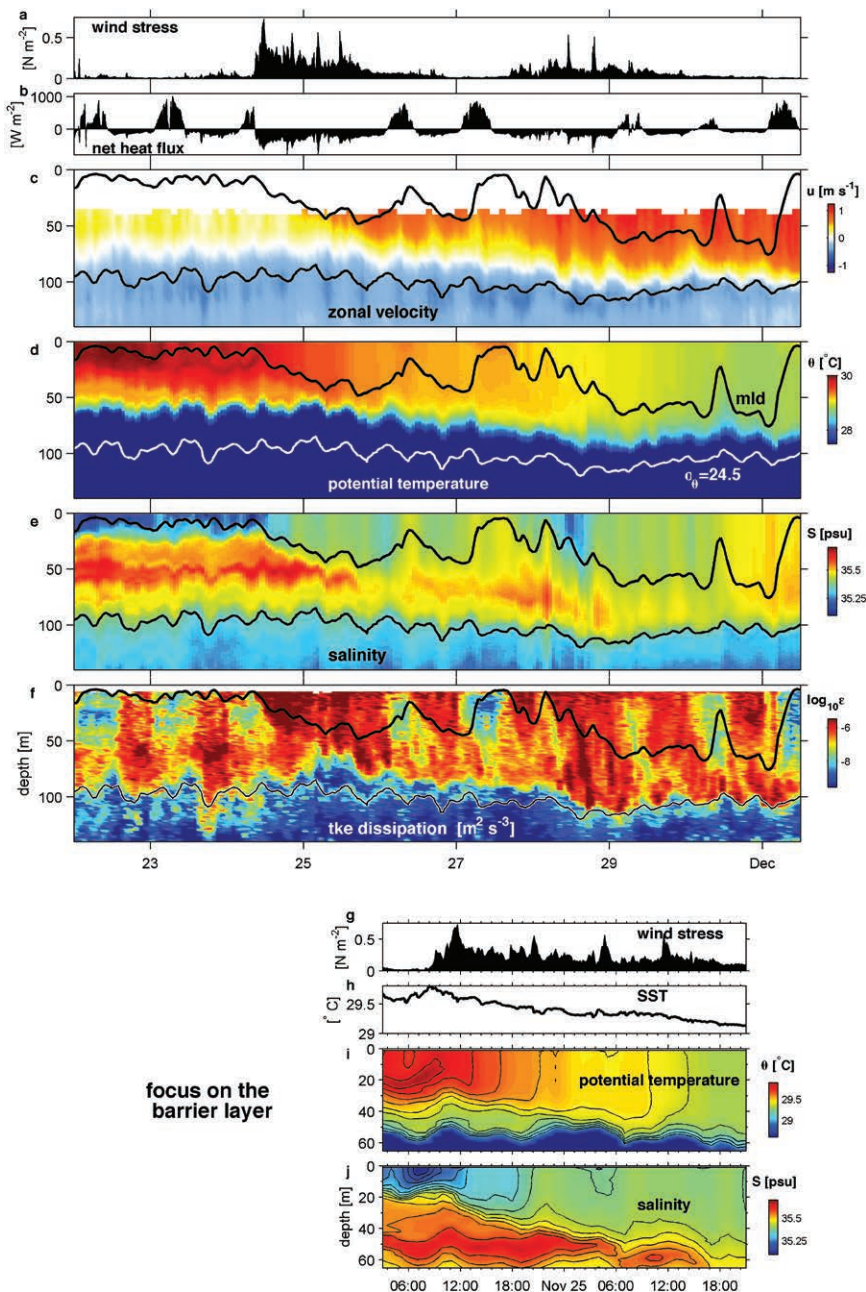
FIG. 7. Summary time series of upper-ocean response to the first westerly wind burst of MJO2 at *Revelle* on 24 Nov 2011. (a) The wind stress (total) appears as a step function change from near-0 to 0.5 N m^{-2} in a few minutes. (b) Net surface heating. Net surface cooling lasted for more than one day, a rarity at the equator, though common during the passage of MJO events. (c) Zonal current. The eastward surface current (the Yoshida–Wyrtki jet) accelerated from <0.5 m s^{-1} in about one day, deepening with time. The mixed layer is indicated by the black line, the potential density surface 1024.5 is indicated by the white line. (d) Temperature. Mixed-layer cooling was driven by combined atmospheric and subsurface cooling. (e) Salinity. Salinification of the surface was driven by an excess of subsurface mixing over precipitation. (f) Turbulence dissipation. (bottom) Expanded plots showing the first 24 h following arrival of the wind burst. (g) Wind stress. (h) SST (cool skin correction applied). (i) Temperature with temperature contours scaled to represent identical contribution to density. (j) Salinity, with contours scaled as in (i).

depth in the first 24 h after the arrival of the wind burst.

In the Pacific and Atlantic Oceans, steady equatorial easterlies drive a westward surface current. Steady easterlies do not exist in the equatorial Indian Ocean, where reversing zonal winds cause intermittent amplification of an eastward-flowing surface current at the equator known as the Yoshida–Wyrtki jet (Yoshida 1959; Wyrtki 1973). Nagura and McPhaden (2008) described the roughly linear dynamics by which the zonal acceleration is balanced by the surface wind stress and pressure gradient force.

In the wake of MJO2, the details of the Yoshida–Wyrtki jet spinup process were observed in greater detail than has previously been possible. Before the arrival of WWB1, a weak eastward zonal surface current overlaid a westward undercurrent (only the top of the undercurrent is seen in Fig. 7c). In the first two days following the arrival of WWB1, the mixed layer cooled by almost 1°C because of the combination of atmospheric cooling from above and mixing

from below, which is roughly partitioned as 2/3 temperature change contribution from the atmosphere and 1/3 from the ocean [based on turbulence heat flux estimates following Moum et al. (2009)]. The mixed layer deepened to 50 m after WWB1 and deepened further after WWB2. The Yoshida–Wyrtki jet accelerated (Fig. 7 and sidebar on the evolving cross-equatorial structure of the Yoshida–Wyrtki jet) to speeds in excess of 1 m s^{-1}, due almost solely to the excess of wind stress over turbulent friction at the base of the jet. Subsequent slow deceleration of the jet following WWB2 was approximately in balance with shear-generated turbulent friction at its base.

SUMMARY. The previous large-scale intensive tropical air–sea interaction experiment, the Tropical Ocean Global Atmosphere Coupled Ocean–Atmosphere Response Experiment (TOGA COARE; 1992–93) was designed to observe the evolution of the MJO as it propagated into the western equatorial Pacific warm pool. TOGA COARE provided

EVOLVING CROSS-EQUATORIAL STRUCTURE OF THE YOSHIDA–WYRTKI JET

Cross-equatorial transects of upper-ocean currents measured using hull-mounted Doppler sonars were executed across 80.5°E on 3 October, 10 November, and 3 December 2011 during passage to and from *Revelle*'s equatorial station (Fig. SB3). These reveal the broad nature of the acceleration of zonal currents following the westerly wind bursts of MJO2 and hint at the deceleration processes thereafter.

The contrast between Figs. SB3a and SB3b is due almost completely to the wind-induced acceleration depicted in

Fig. 7. Zonal velocities increased throughout the 4° longitude band straddling the equator, leading to a doubling of the volumetric transport in the eastward direction. The reason for the shallowing, weakening, and broadening of the westward-flowing undercurrent (Fig. SB3c; ~180–300-m depth) is unclear but may represent a local thermocline response to the wind bursts. In this scenario, the greatly increased current shear at the base of the eastward Yoshida–Wyrtki jet contributes to stratified shear instability through reduction of the gradient Richardson number (proportional to the ratio of vertical gradients of density and velocity; e.g., Smyth et al. 2011). Resulting high turbulence levels carry eastward momentum down from the surface current and contribute to sea surface cooling for an extended period following the passage of MJO2.
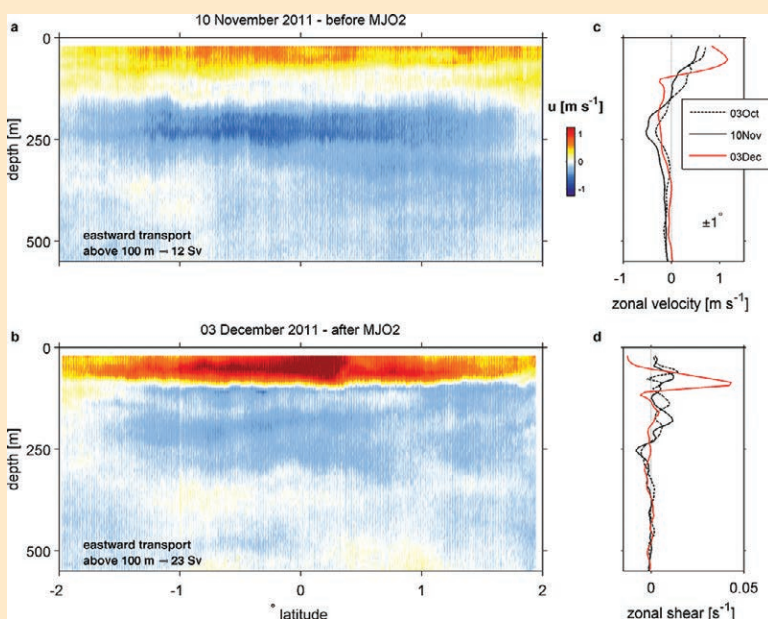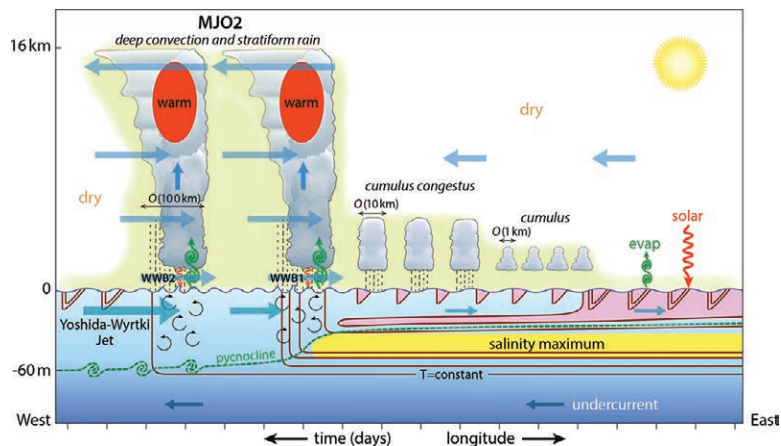

FIG. SB3. Cross-equatorial structure of zonal currents at 80°E from 2°S to 2°N (a) before and (b) following the westerly wind burst during MJO2. Eastward transports represent the volumetric flow rate through the cross section above 100 m in units of Sverdrups (1 Sv = 10^6 m^3 s^{-1}). c) Average velocity profiles between 1°S and 1°N on 3 Oct, 10 Nov, and 3 Dec. (d) Corresponding average profiles of zonal current shear *du/dz*.

observations of an evolved state of the MJO with some of the same types of measurements deployed in DYNAMO. The DYNAMO field campaign targeted the MJO at an earlier phase in its evolutionary cycle using a more complete and modern suite of measurements, including new observations described here (e.g., the development of the surface wave field and the injection of aerosols into the marine boundary layer) and some not (e.g., high-resolution Doppler lidar scanning of the atmospheric boundary layer), as well as improved sampling (eight soundings per day in DYNAMO compared to four per day in TOGA COARE). The combination of these measurements provides an unprecedented observational dataset extending from 1 km beneath the sea surface to 25 km above, with increased

FIG. 8. Schematic showing processes observed during MJO2 at 0°, 80°E in November 2011. The upper 150 m of the ocean and lower 16 km of the atmosphere are represented as a right-to-left linear time series. This might also be considered a zonal transect along the equator. Green shading in the atmosphere indicates moist air. Pink shading in the ocean indicates the warmest waters, outlined by red isotherms. Near-surface triangles denote diurnal warm layers, with their intensity proportional to the number of isotherms.

concentration of measurements near the sea surface, and is in the process of being assembled and quality controlled for future generations. These data represent detailed observations of the internal structure of convectively coupled Kelvin waves embedded in an MJO; their influence on the ocean; and the broad cross-equatorial structure, long-lasting effect, and potential feedbacks caused by Yoshida–Wyrtki jets.

We note a few general tendencies of the three realizations of the MJO observed during the DYNAMO field campaign. All three MJO active-phase events were characterized by low OLR that roughly matched the time scale of the low surface pressure signal at *Revelle*. During the suppressed phases, SST and oceanic heat storage rose day by day. SST exhibited a marked diurnal cycle under low winds, sunny skies, and inhibited atmospheric convection shading only a limited area of the sea surface.

MJO2 offers a vivid example of the changes brought to the ocean–atmosphere system by the active phase, summarized schematically in Fig. 8. During the dry, suppressed phase (far right of Fig. 8), excess solar heating over evaporative cooling creates intense diurnally varying warm layers (1–3 K) in the upper 5–10 m of the ocean. The active phase begins with progressively deeper and wetter cloud systems. These reduce solar heating at the surface, thereby reducing diurnal warm-layer amplitude; consequently, daily-averaged SST plateaus prior to the arrival of the wind bursts. The remnant warm layer above the pycnocline

is part of the barrier-layer structure maintained by preexisting salinity stratification.

The active phase of MJO2 is clearly defined by the two distinctive westerly wind bursts–rain events (far left of Fig. 8), each associated with propagating atmospheric disturbances (Fig. 3). These lasted six days, separated by a 24-h quiescent period. Warming of the deep troposphere was consistent with the shift in the precipitating cloud population: from convective precipitation covering a limited area, to intense deep convection briefly, and then to widespread stratiform precipitation with weak embedded convection. The stratiform rain pattern persisted for two days in each event, during which widespread cloudiness significantly reduced the solar radiation reaching the sea surface. A deep (up to 8 km height) westerly wind anomaly developed following the heating in the upper troposphere. Westerly wind anomalies at the surface synchronous with the stratiform rain are consistent with zonal convergence supplying mass to updrafts fueled by latent heat of condensation. These convective updrafts fed the stratiform precipitation. It is not known at this time what role the large-scale convergence alone may have played in creating or enhancing stratiform precipitation.

The combination of buoyancy forcing (excess evaporative cooling over solar heating) plus wind stress mixed the upper ocean. SST decreased rapidly in response to the cumulative cooling by surface fluxes plus subsurface mixing. These upward

turbulent heat fluxes contributed to the destabilization of the atmosphere during the active phase. Since the associated wind bursts also accelerated the Yoshida–Wyrtki jet, the oceanic contribution to the near-surface heat budget was sustained beyond the passage of the wind bursts because of shear-induced turbulence and mixing across the thermocline at the jet base. Sustained deep mixing from this turbulence limited the SST increase in the subsequent suppressed phase. We note that recovery of SST following the relatively weak MJO1 (in terms of magnitude and rate of change of OLR and surface pressure; Fig. 2d) was rapid and intense and was followed by a relatively strong MJO2. After MJO2, weaker SST recovery was followed by a relatively weak MJO3. An obvious issue that must be addressed is the potential role of this effect in retarding the formation and/or intensity of subsequent active-phase events.

REFERENCES

Balaguru, K., P. Chang, R. Saravan, L. R. Leung, M. Liu, and J.-S. Hsieh, 2012: Ocean barrier layers' effect on tropical cyclone intensification. *Proc. Natl. Acad. Sci. USA,* **109,** 14 343–14 347, doi:10.1073/pnas.1201364109.

Bates, T. S., P. K. Quinn, D. J. Coffman, J. E. Johnson, and A. M. Middlebrook, 2005: Dominance of organic aerosols in the marine boundary layer over the Gulf of Maine during NEAQS 2002 and their role in aerosol light scattering. *J. Geophys. Res.,* **110,** D18202, doi:10.1029/2005JD005797.

Bell, T. L., and R. Suhasini, 1994: Principal modes of variation of rain-rate probability distribution. *J. Appl. Meteor.,* **33,** 1067–1078, doi:10.1175/1520-0450(1994)0332.0.CO;2.

Borge, J. C. N., K. Reichert, and J. Dittmer, 1999: Use of nautical radar as a wave monitoring instrument. *Coastal Eng.,* **37,** 331–342, doi:10.1016/S0378-3839(99)00032-0.

Cifuentes-Lorenzen, A., J. B. Edson, C. J. Zappa, and L. Bariteau, 2013: A multisensor comparison of ocean wave frequency spectra from a research vessel during the Southern Ocean Gas Exchange Experiment. *J. Atmos. Oceanic Technol.,* **30,** 2907–2925, doi:10.1175/JTECH-D-12-00181.1.

DeWitt, H. L., D. J. Coffman, K. J. Schulz, W. A. Brewer, T. S. Bates, and P. K. Quinn, 2013: Atmospheric aerosol properties over the equatorial Indian Ocean and the impact of the Madden-Julien oscillation. *J. Geophys. Res.,* **118,** 5736–5749, doi:10.1002/jgrd.50419.

Fairall, C. W., E. F. Bradley, J. S. Godfrey, J. B. Edson, G. S. Young, and G. A. Wick, 1996: Cool skin and warm layer effects on the sea surface temperature. *J. Geophys. Res.,* **101,** 1295–1308, doi:10.1029/95JC03190.

Gottschalck, J., P. E. Roundy, C. J. Schreck III, A. Vintzileos, and C. Zhang, 2013: Large-scale atmospheric and oceanic conditions during the 2011–12 DYNAMO field campaign. *Mon. Wea. Rev.,* **141,** 4173–4196, doi:10.1175/MWR-D-13-00022.1.

Johnson, R. H., and P. E. Ciesielski, 2013: Structure and properties of Madden–Julian oscillations deduced from DYNAMO sounding arrays. *J. Atmos. Sci.,* **70,** 3157–3179, doi:10.1175/JAS-D-13-065.1.

Kiladis, G. N., M. C. Wheeler, P. T. Haertel, K. H. Straub, and P. E. Roundy, 2009: Convectively coupled equatorial waves. *Rev. Geophys.,* **47,** RG2003, doi:10.1029/2008RG000266.

Köhler, H., 1936: The nucleus in and the growth of hydroscopic droplets. *Trans. Faraday Soc.,* **32,** 1152–1161, doi:10.1039/tf9363201152.

Madden, R., and P. Julian, 1971: Detection of a 40-50 day oscillation in the zonal wind in the tropical Pacific. *J. Atmos. Sci.,* **28,** 702–708, doi:10.1175/1520-0469(1971)0282.0.CO;2.

——, and ——, 1972: Description of global-scale circulation cells in the tropics with a 40-50 day period. *J. Atmos. Sci.,* **29,** 1109–1123, doi:10.1175/1520-0469(1972)0292.0.CO;2.

McPhaden, M. J., and G. R. Foltz, 2013: Intraseasonal variations in the surface heat layer balance of the central equatorial Indian Ocean: The importance of zonal advection and vertical mixing. *Geophys. Res. Lett.,* **40,** 2737–2741, doi:10.1002/grl.50536.

——, and Coauthors, 2009: RAMA—The Research Moored Array for African–Asian–Australian Monsoon Analysis and Prediction. *Bull. Amer. Meteor. Soc.,* **90,** 459–480, doi:10.1175/2008BAMS2608.1.

Moreno, G., L. Dagorn, G. Sancho, and D. Itano, 2007: Fish behaviour from fishers' knowledge: The case study of tropical tuna around drifting fish aggregating devices (DFADs). *Can. J. Fish. Aquat. Sci.,* **64,** 1517–1528, doi:10.1139/f07-113.

Moum, J. N., M. C. Gregg, R.-C. Lien, and M. E. Carr, 1995: Comparison of turbulent kinetic energy dissipation rates from two ocean microstructure profilers. *J. Oceanic Atmos. Technol.,* **12,** 346–366, doi:10.1175/1520-0426(1995)0122.0.CO;2.

——, R.-C. Lien, A. Perlin, J. N. Nash, M. C. Gregg, and P. J. Wiles, 2009: Sea surface cooling at the equator by subsurface mixing in tropical instability waves. *Nat. Geosci.,* **2,** 761–765, doi:10.1038/ngeo657.

Nagura, M., and M. J. McPhaden, 2008: The dynamics of zonal current variations in the central equatorial Indian Ocean. *Geophys. Res. Lett.,* **35,** L23603, doi:10.1029/2008GL035961.

Petters, M. D., and S. M. Kreidenweis, 2007: A single particle representation of hygroscopic growth and cloud condensation nucleus activity. *Atmos. Chem. Phys.,* **7,** 1961–1971, doi:10.5194/acp-7-1961-2007.

Rosenfeld, D., U. Lohman, G. B. Raga, C. D. O'Dowd, M. Kulmala, S. Fuzzi, A. Reissell, and M. O. Andreae, 2008: Flood or drought: How do aerosols affect precipitation? *Science,* **321,** 1309–1313, doi:10.1126/science.1160606.

Roundy, P. E., 2008: Analysis of convectively-coupled Kelvin waves in the Indian Ocean MJO. *J. Atmos. Sci.,* **65,** 1342–1359, doi:10.1175/2007JAS2345.1.

Schumacher, C., R. A. Houze, and I. Kraucunas, 2004: The tropical dynamical response to latent heating estimates derived from TRMM precipitation radar. *J. Atmos. Sci.,* **61,** 1341–1358, doi:10.1175/1520-0469(2004)0612.0.CO;2.

Short, D. A., P. A. Kucera, B. S. Ferrier, J. C. Gerlach, S. A. Rutledge, and O. W. Thiele, 1997: Shipboard radar rainfall patterns within the TOGA COARE IFA. *Bull. Amer. Meteor. Soc.,* **78,** 2817–2836, doi:10.1175/1520-0477(1997)0782.0.CO;2.

Smyth, W. D., J. N. Moum, and J. D. Nash, 2011: Narrowband high-frequency oscillations at the equator. Part II: Properties of shear instabilities. *J. Phys. Oceanogr.,* **41,** 412–428, doi:10.1175/2010JPO4451.1.

Steiner, M., R. A. Houze, and S. A. Yuter, 1995: Climatological characterization of three-dimensional storm structure from operational radar and rain gauge data. *J. Appl. Meteor.,* **34,** 1978–2007, doi:10.1175/1520-0450(1995)0342.0.CO;2.

Straub, K. H., and G. N. Kiladis, 2002: Observations of a convectively coupled Kelvin wave in the eastern Pacific ITCZ. *J. Atmos. Sci.,* **59,** 30–53, doi:10.1175/1520-0469(2002)0592.0.CO;2.

Wyatt, L. R., and Coauthors, 2003: Validation and intercomparisons of wave measurements and models during the EuroROSE experiments. *Coastal Eng.,* **48,** 1–28, doi:10.1016/S0378-3839(02)00157-6.

Wyrtki, K., 1973: An equatorial jet in the Indian Ocean. *Science,* **181,** 262–264, doi:10.1126/science.181.4096.262.

Yoneyama, K., C. Zhang, and C. N. Long, 2013: Tracking pulses of the Madden–Julian oscillation. *Bull. Amer. Meteor. Soc.,* **94,** 1871–1891, doi:10.1175/BAMS-D-12-00157.1.

Yoshida, K., 1959: A theory of the Cromwell Current (the equatorial undercurrent) and of the equatorial upwelling—An interpretation in a similarity to a coastal circulation. *J. Oceanogr. Soc. Japan,* **15,** 159–170.

Yuter, S. A., and R. A. Houze, 1998: The natural variability of precipitating clouds over the western Pacific warm pool. *Quart. J. Roy. Meteor. Soc.,* **124,** 53–99, doi:10.1002/qj.49712454504.

Zhang, C., 2005: Madden-Julian oscillation. *Rev. Geophys.,* **43,** RG2003, doi:10.1029/2004RG000158.

——, 2013: Madden–Julian oscillation: Bridging weather and climate. *Bull. Amer. Meteor. Soc.,* **94,** 1849–1870, doi:10.1175/BAMS-D-12-00026.1.